# KINETIC AND THERMODYNAMIC INSIGHTS INTO THE HYDROGENOLYSIS OF FERROCENE

A.I. Rustamova<sup>1\*</sup>, S.N. Osmanova<sup>1,2</sup>, F.K. Pashayeva<sup>1</sup>, R.H. Aghayeva<sup>1</sup>, V.M. Ahmadov<sup>1</sup>, A.N. Mammadov<sup>1,3</sup>, S. Bellucci<sup>4,5</sup>, E.H. Ismailov<sup>1</sup>

<sup>1</sup>Institute of Catalysis and Inorganic Chemistry, 113, H. Javid, Az1143, Baku, Azerbaijan, 
<sup>2</sup>Khazar University, 41 Mahsati Str., AZ1096, Baku, Azerbaijan, 
<sup>3</sup>Azerbaijan Technical University, H. Javid Ave. 25, AZ1073, Baku, Azerbaijan, 
<sup>4</sup>National Institute of Materials Physics, Magurele, Romania 
<sup>5</sup>RAIT88 srl, Roma, Italy

\*e-mail: aygun.rustamova1601@gmail.com

Received 03.02.2025 Accepted 29.05.2025

**Abstract:** The thermal reduction of ferrocene in a hydrogen atmosphere was investigated over the temperature range of 573-1173 K, focusing on both the gaseous and solid products formed during the process. The gasphase products (hydrocarbons) and solid products (nanosized iron particles) formed during the reaction were identified. It was shown that, in contrast to the pyrolysis of ferrocene, which produces nanosized iron particles, iron carbide, and carbon, the thermal decomposition of ferrocene in a hydrogen flow yields only nanosized iron particles as the solid product. Furthermore, it was observed that the presence of hydrogen during decomposition leads to the formation of smaller nuclei, which enhances the initiation and growth of nanoparticles more intensively. FMR spectra and X-ray diffraction patterns of the solid residues from the thermal decomposition of ferrocene were obtained and analyzed. The dependence of these patterns on the conditions of thermal decomposition was also demonstrated. The presented results provide direct experimental evidence of the initial stages of the decomposition of  $Fe(C_5H_5)_2$  through detailed analysis of the gas-phase composition. These findings can be applied to improve the modeling of processes involved in the growth of ultra-high-temperature materials (UHTs) and thin films, thereby enabling more efficient synthesis of nanomaterials.

**Keywords:** thermal reduction of ferrocene, gas-phase and solid-phase products, iron nanoparticles, iron carbide, X-ray diffraction, ferromagnetic resonance (FMR)

#### 1. Introduction

Ferrocene (Fe(Cp)<sub>2</sub>), first identified in the second half of the 20th century [1, 2], has become a prominent model compound in organometallic chemistry due to its unique structural and physical properties [3, 4]. It consists of an iron atom sandwiched between two cyclopentadienyl rings in a stable configuration. Ferrocene is characterized by its moderate vapor pressure, air stability at room temperature, and low toxicity, making it an ideal and safe material for the development of functional materials [5, 6]. One of its primary applications is in the synthesis of iron-containing thin films, which have been successfully incorporated into optoelectronic systems [7, 8] and produced in oxidizing environments [9]. Upon thermal decomposition, ferrocene releases iron, leading to the formation of nanoparticles (NPs) that are valuable in various energy-related technologies [10, 11]. Iron nanoparticles (NPs) can serve dual roles as both catalysts in chemical transformations and as active components in magnetic nanostructures. At elevated temperatures, the catalytic activity of iron promotes the growth of carbon-based nanomaterials, such as nanotubes and nanoparticles [12, 13]. In these processes, iron facilitates the decomposition of hydrocarbons, encouraging carbon deposition on its surface [14]. Over the past few decades, iron nanoparticles have gained prominence across multiple disciplines, including data storage, environmental cleanup, catalysis, and biomedical applications. Of particular interest are metallic iron and its oxides [15, 16]. While iron oxides are biocompatible and environmentally stable, their magnetic performance diminishes at the nanoscale. To improve their properties, core-shell structures have been developed by passivating iron NPs, enhancing their stability and magnetic characteristics [17, 18].

The thermal decomposition of ferrocene has been observed to occur within a temperature range of 673–1073 K under oxidizing, reducing, or inert gas conditions [19–21]. During pyrolysis, ferrocene breaks down, releasing hydrocarbon fragments, elemental carbon, and iron-based particles. When hydrogen is present, these hydrocarbon intermediates and carbon residues can undergo further reactions, resulting in the formation of low-molecular-weight hydrocarbons such as methane and ethane. Investigating the hydrogenolysis and pyrolysis of ferrocene-especially from thermodynamic and kinetic perspectives, as well as with a focus on nanoparticle formation and control—is critical for two main reasons. First, ferrocene (Fe(C<sub>5</sub>H<sub>5</sub>)<sub>2</sub>) is a readily available, air-stable iron compound that serves both as a convenient precursor and a dual source of nanoscale iron and carbon. Second, iron and iron carbide nanoparticles (Fe, Fe<sub>3</sub>C) are of considerable interest in catalysis and advanced materials research. These nanomaterials have demonstrated excellent catalytic activity in processes such as Fischer–Tropsch (FT) synthesis, hydrogenation of CO and CO<sub>2</sub>, hydrocarbon reforming, and the production of carbon nanostructures, including carbon nanotubes and graphene-like materials. Such applications underscore the importance of methods that allow precise control over nanoparticle synthesis [22, 23].

In this study, we examine the kinetic and thermodynamic behavior of ferrocene hydrogenolysis over a temperature range of 573–1173 K. The composition of the gaseous reaction products was characterized using a microreactor setup equipped with mass spectrometry and online gas chromatography. Meanwhile, solid-phase products were analyzed using X-ray diffraction (XRD) and ferromagnetic resonance (FMR) spectroscopy. A key aim of this work is to explore strategies for the controlled synthesis of iron nanoparticles with adjustable size distributions, which could enable future development of supported catalyst systems (e.g., on Al<sub>2</sub>O<sub>3</sub>, SiO<sub>2</sub>, or ZrO<sub>2</sub>) for various catalytic applications.

## 2. Experimental part

Fig. 1 presents the overall view and schematic diagram of an integrated microreactor–mass spectrometer system, produced by Hiden Analytical (UK) and installed at the Institute of Catalysis and Inorganic Chemistry in April 2022, which has been used to study this reaction. Using this system, real-time measurements were taken up to 1173 K, and gas-phase products of the thermal decomposition reaction of ferrocene in hydrogen and inert gas (N<sub>2</sub>) flow in the range of 573-1173 K (H<sub>2</sub>, N<sub>2</sub>, CH<sub>4</sub>, C<sub>2</sub>H<sub>4</sub>, C<sub>2</sub>H<sub>6</sub>, C<sub>3</sub>H<sub>6</sub>, n-C<sub>3</sub>H<sub>8</sub>, n-C<sub>4</sub>H<sub>10</sub>, n-C<sub>5</sub>H<sub>12</sub>, n-C<sub>6</sub>H<sub>14</sub>, C<sub>2</sub>H<sub>2</sub>, C<sub>5</sub>H<sub>6</sub> and dicyclopenthadiene) were identified.

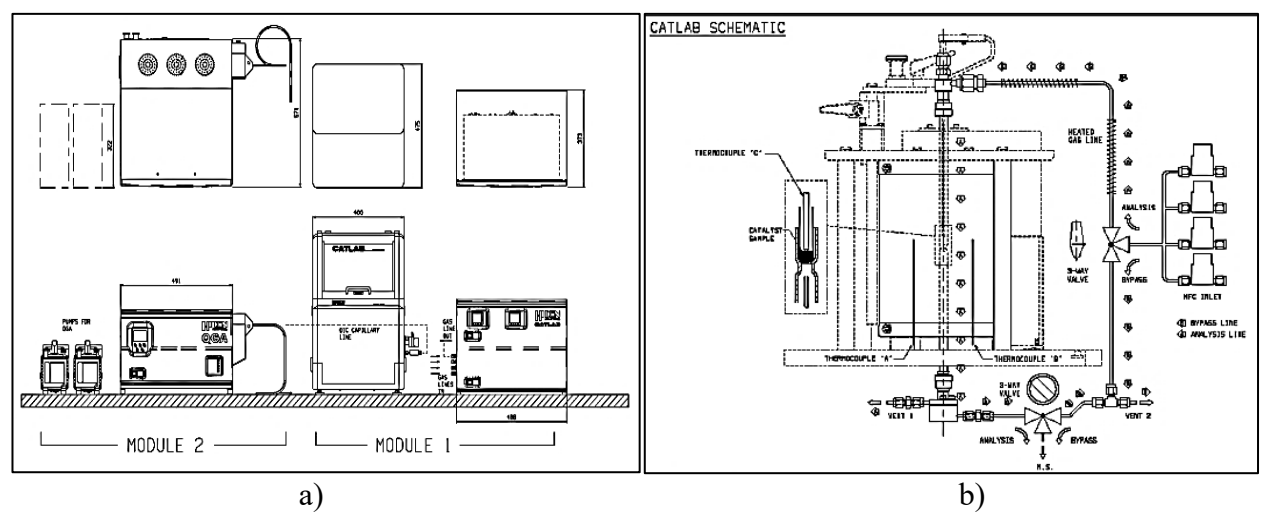


**Fig. 1**. (a) General view and (b) schematic diagram of the Catlab complex from Hiden Analytical Ltd., UK, which consists of a microreactor coupled to a mass spectrometer

The reaction products were continuously analyzed using an Agilent 7820A gas chromatograph (GC), equipped with a flame ionization detector (FID) and a 30-meter ZB-624 capillary column with

a 0.53 mm internal diameter. A schematic representation of the laboratory setup used for the ferrocene reduction experiment is provided in Fig. 2.

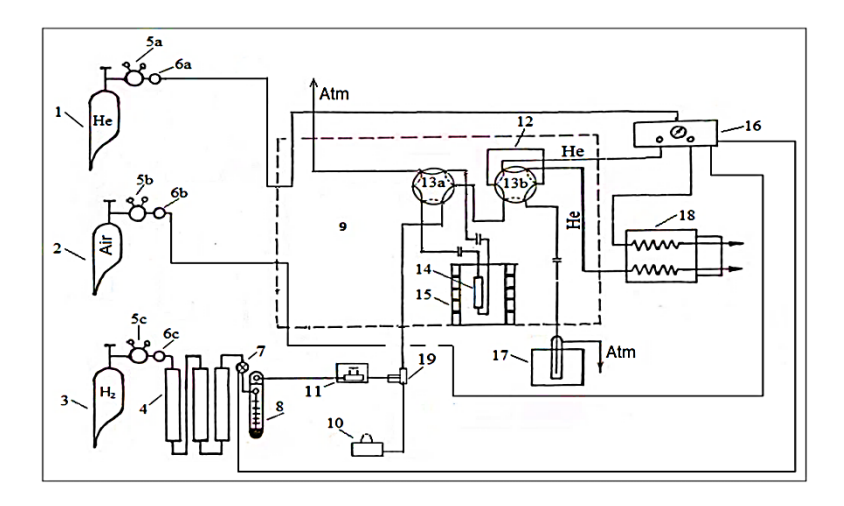


**Fig. 2.** A schematic diagram of the experimental laboratory setup designed for the thermal reduction of ferrocene is presented below. The system includes the following components: 1– Helium balloon; 2 – Air balloon; 3 – Hydrogen ballon; 4 – Hydrogen purification columns; 5a, 5b, 5c – Dual-chamber pressure regulators; 6a, 6b, 6c – low-pressure regulator; 7 – Precision gas flow control valve; 8 – capillary rheometer; 9 – thermostat; 10 – microsyringe pump; 11– Syring pump; 12 – sample loop; 13a, 13b – Six-way switching valves; 14 – Reaction chamber; 15 – electric furnace; 16 – gas preparation unit for chromatography; 17 – reaction product collector; 18 – chromatograph; 19 – Three-way gas line for feeding hydrogen and the reactant mixture into the system. The gas chromatographic analysis was performed using an Agilent 7820A GC equipped with a flame ionization detector (FID). v(He flow rate) = 15 ml/min; v (Air)= 300 ml/min; v (H<sub>2</sub>) = 30 ml/min; T (Detector)– 573 K; T(Inlet) – 523 K; P(Inlet) – 1.2598 psi; Oven temperature range: 313–453 K; ZB-624 capillary column l = 30 m; d = 0.53 mm; He pressure in the capillary column – 1.2598 psi.

The hydrogenolysis of ferrocene Fe(Cp)<sub>2</sub> was carried out under the following experimental conditions: A total of 0.3 g of pre-synthesized, finely divided ferrocene was loaded into a reaction tube situated within a thermostatically controlled furnace. The furnace, equipped with an electric heating element, contained the ferrocene sample positioned between two quartz grain layers. The reaction proceeded in a continuous flow mode. To monitor the reaction temperature, a thermocouple was placed at the center of the catalyst layer, with temperature regulation managed by a Micromax microelectronic controller. The hydrogenolysis was carried out within a temperature range of 573–873 K, with a hydrogen flow rate of 15 mL/min.

The solid products formed at the end of the reaction were identified using an X-ray diffractometer (XRD D2) and an EPR spectrometer (EMXmicro) from Bruker, Germany.

### 3. Results and discussion

Fig.s 3a-b show the chromatograms of the gas-phase products of ferrocene thermolysis in a hydrogen flow at 573 and 773 K.

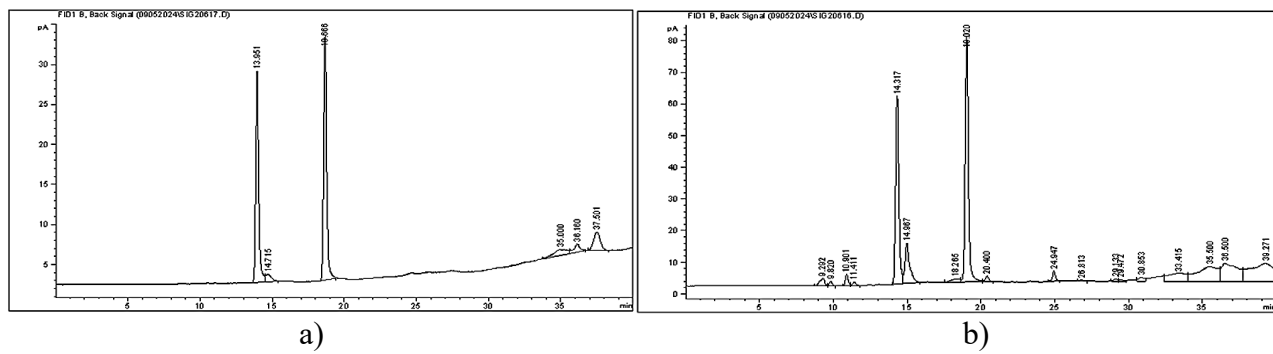


**Fig. 3a, b.** Chromatograms of the gas-phase products of ferrocene thermolysis in a hydrogen flow: a) 573 K and b) 773 K

Table 1 presents the data from mass spectrometric and chromatographic analyses of the gasphase products of the ferrocene hydrogenolysis reaction.

**Table 1.** Mass spectrometric and chromatographic analysis data on the composition of gas-phase products of the ferrocene hydrogenolysis reaction

Temperature, K	Gas Phase products of ferrocene hydrogenolysis
573-673	C <sub>5</sub> H <sub>6</sub> (70%), CH <sub>4</sub> (15%), H <sub>2</sub> (10%), C <sub>2</sub> H <sub>4</sub> (4%), C <sub>2</sub> H <sub>2</sub> (1%)
773	C <sub>5</sub> H <sub>6</sub> (55%), CH <sub>4</sub> (25%), H <sub>2</sub> (12%),C <sub>2</sub> H <sub>4</sub> (6%), C <sub>2</sub> H <sub>2</sub> (2%)
873	C <sub>5</sub> H <sub>6</sub> (40%), CH <sub>4</sub> (30%), H <sub>2</sub> (15%),C <sub>2</sub> H <sub>4</sub> (10%), C <sub>2</sub> H <sub>2</sub> (5%)
973	C <sub>5</sub> H <sub>6</sub> (25%), CH <sub>4</sub> (35%), H <sub>2</sub> (20%),C <sub>2</sub> H <sub>4</sub> (13%), C <sub>2</sub> H <sub>2</sub> (7%)
1073	C <sub>5</sub> H <sub>6</sub> (15%), CH <sub>4</sub> (37%), H <sub>2</sub> (25%),C <sub>2</sub> H <sub>4</sub> (15%), C <sub>2</sub> H <sub>2</sub> (8%)
1173	C <sub>5</sub> H <sub>6</sub> (5%), CH <sub>4</sub> (39%), H <sub>2</sub> (30%),C <sub>2</sub> H <sub>4</sub> (18%), C <sub>2</sub> H <sub>2</sub> (8%)

Table 1 presents the composition of the main identified gas-phase products of the ferrocene hydrogenolysis reaction in the temperature range from 573 K to 1173 K. The features of ferrocene thermolysis are as follows: cyclopentadiene dominates at low temperatures (573–673 K) and then gradually decomposes; CH<sub>4</sub> and H<sub>2</sub> are formed increasingly as the temperature rises; C<sub>2</sub>H<sub>4</sub> and C<sub>2</sub>H<sub>2</sub> (decarbonization fragments) primarily appear at temperatures >873 K. The obtained results are in good agreement with literature data, for example, reference [22].

At low temperatures (573–673 K), the primary decomposition products, such as cyclopentadiene (C<sub>5</sub>H<sub>6</sub>) and its radicals, predominate. C<sub>5</sub>H<sub>6</sub> (cyclopentadiene) dominates in this temperature range but rapidly decomposes upon further heating. As the temperature increases, the proportion of secondary products such as methane (CH<sub>4</sub>), hydrogen (H<sub>2</sub>), ethylene (C<sub>2</sub>H<sub>4</sub>), and acetylene (C<sub>2</sub>H<sub>2</sub>) rises, indicating further decomposition of the primary products. The amounts of CH<sub>4</sub> and H<sub>2</sub> increase sharply with temperature, reaching a maximum in the range of 973–1173 K. C<sub>2</sub>H<sub>4</sub> and C<sub>2</sub>H<sub>2</sub> are formed predominantly at high temperatures (>873 K), and their formation indicates secondary fragmentation of carbon-containing fragments. At temperatures above 973 K, enhanced formation of iron nanoparticles is observed. Along with these, solid thermolysis products such as iron carbide (Fe<sub>3</sub>C) and nanoscale carbon particles are also formed, as confirmed by XRD and FMR studies.

Table 2 presents the main differences in the composition of the products of ferrocene hydrogenolysis and pyrolysis.

**Table 2.** Comparison of the Product Composition in Ferrocene Hydrogenolysis and Pyrolysis

Temperature, K	Hydrogenolysis	Pyrolysis
573-673	High yield of C5H6,	A similar, but less H <sub>2</sub> and more C <sub>2</sub> H <sub>4</sub>
	small amounts of CH <sub>4</sub> and H <sub>2</sub>	
773-873	Increase in CH <sub>4</sub> , H <sub>2</sub>	More C <sub>2</sub> H <sub>4</sub> and C <sub>2</sub> H <sub>2</sub> , less H <sub>2</sub>
973–1173	Prevalence of CH <sub>4</sub> , H <sub>2</sub>	Prevalence of C <sub>2</sub> H <sub>4</sub> , C <sub>2</sub> H <sub>2</sub>

Thus, it can be concluded that hydrogenolysis in the presence of H<sub>2</sub> suppresses fragmentation and leads to the formation of small molecules of saturated hydrocarbons, primarily methane (CH<sub>4</sub>) and hydrogen (H<sub>2</sub>), while pyrolysis promotes dehydrogenation and the formation of unsaturated fragments (C<sub>2</sub>H<sub>4</sub>, C<sub>2</sub>H<sub>2</sub>) and carbon residues.

The presence of hydrogen (H<sub>2</sub>) in the gas-phase products of ferrocene hydrogenolysis may seem paradoxical at first, since hydrogenolysis occurs in a hydrogen flow. However, the inclusion of H<sub>2</sub> in the product mixture is justified for the following reasons:

The cleavage of Fe-C bonds is accompanied by the formation of cyclopentadienyl fragments (C<sub>5</sub>H<sub>5</sub>\*), which react with H<sub>2</sub> to produce C<sub>5</sub>H<sub>6</sub>, CH<sub>4</sub>, C<sub>2</sub>H<sub>4</sub> and secondary H<sub>2</sub>. These fragments can also undergo further fragmentation, releasing atomic hydrogen, which then recombines to form molecular H<sub>2</sub>. Thus, H<sub>2</sub> can arise as a reaction product, not only as an external reagent.

At high temperatures,  $C_5H_6$ ,  $CH_4$ , and other fragments may lose  $H_2: C_xH_y \rightarrow C_xH_{y-2} + H_2$ .

This is especially characteristic for the formation of unsaturated hydrocarbons (C<sub>2</sub>H<sub>4</sub>, C<sub>2</sub>H<sub>2</sub>), each of which is accompanied by the release of hydrogen. Therefore, it can be concluded that hydrogen is present in the gas-phase products of hydrogenolysis because it can be generated during the thermolysis of ferrocene and secondary reactions (secondary H<sub>2</sub>). The final hydrogenolysis equation, without accounting for the formation of iron carbide and several hydrocarbons, can be written as:

$$2Fe(C_5H_5)_2 + 2H_2 \rightarrow 2Fe + 2CH_4 + 2C_2H_2 + 2C_5H_6 + 4C(s)$$

Let us emphasize once again that the formation of unsaturated hydrocarbons (such as ethylene C<sub>2</sub>H<sub>4</sub> and acetylene C<sub>2</sub>H<sub>2</sub>) during the hydrogenolysis of ferrocene is related to the thermal and catalytic pathways of dehydrogenation of the fragments formed during the breakdown of the cyclopentadienyl rings.

The results of thermodynamic analysis of the reactions of thermal decomposition of ferrocene in a stream of inert gas  $(N_2)$  and hydrogen in the temperature range of 293–1173 K are given below.

```
(C_5H_5)_2Fe(g) \rightarrow Fe(s) + C_{10}H_{10}(g)
                                                                                            (1)
\Delta G_T^0 = 502.9 - 0.150 \text{T} + 0.0298 \text{T} [\ln(\text{T}/298) + (298/\text{T}) - 1]
                                                                                            (1a)
lnK_p = -120.479(502.9 - 0.150T + 0.0298T[ln(T/298) + (298/T) - 1])/T
                                                                                            (1b)
C_{10}H_{10}(g) \rightarrow CH_4(g) + C_2H_4(g) + C_2H_2(g) + 5C(s)
                                                                                            (2)
\Delta G_T^0 = -539 - 0.4019 \text{T} - 0.0789 \text{T} [\ln(\text{T}/298) + (298/\text{T}) - 1]
                                                                                            (2a)
lnK_p = -120.479(-539-0.4019T-0.0789T[ln(T/298)+(298/T)-1])/T
                                                                                            (2b)
(C_5H_5)_2Fe(g) \rightarrow Fe(s) + CH_4(g) + C_2H_4(g) + C_2H_2(g) + 5C(s)
                                                                                            (3)
\Delta G_T^0 = -36.9 - 0.5509 \text{T} - 0.0489 \text{T} [\ln(\text{T}/298) + (298/\text{T}) - 1]
                                                                                            (3a)
lnK_p = -120.479(-36.9 - 0.5509T - 0.0489T[ln(T/298) + (298/T) - 1])/T
                                                                                            (3b)
Fe(C_5H_5)_2(g)+H_2(g) \rightarrow Fe(s)+2C_5H_6(g)
                                                                                            (4)
\Delta G_T^0 = -19.09 + 0.09809 + 0.02921 + [ln(T/298) + (298/T) - 1]
                                                                                            (4a)
\ln K_p = -120.479(-19.09+0.09809T+0.02921T[\ln(T/298)+(298/T)-1])/T
                                                                                            (4b)
2C_5H_6(g) + 8H_2(g) \rightarrow CH_4(g) + C_2H_6(g) + C_3H_8(g) + C_4H_{10}(g)
                                                                                            (5)
\Delta G_T^0 = -606.9 - 0.43558T + 0.2029T[ln(T/298) + (298/T) - 1]
                                                                                            (5a)
lnK_p = -120.479(-606.9 - 0.43558T + 0.2029T[ln(T/298) + (298/T) - 1])/T
                                                                                            (5b)
```

The approximation of the temperature dependences for the Gibbs free energy and the logarithmic values of the equilibrium constant for reactions (1-5) were determined by the method described in [24-26]. Thermodynamic data for the substances involved in reactions (1-5) were taken from sources [27-29]. Thermodynamic data for dicyclopentadienyl C<sub>10</sub>H<sub>10</sub> are not available in the literature, so these parameters were determined based on the thermodynamic properties of

cyclopentadiene, using the C-H bond dissociation energy and the C-C bond formation energy [30]. The following thermodynamic data for C<sub>10</sub>H<sub>10</sub> were obtained:

$$\Delta H_{298}^{0}(C_{10}H_{10},g)=738.97 \text{ kJ/mol},$$
  
 $S_{298}^{0}(C_{10}H_{10},g)=234.88 \text{ J/ mol.K},$   
 $C_{p,298}^{0}(C_{10}H_{10},g)=200.96 \text{ J/ mol.K}$ 

Temperature dependences of the Gibbs free energy and the logarithmic values of the equilibrium constant for reactions (1-5) are shown in Fig.s 4 and 5.

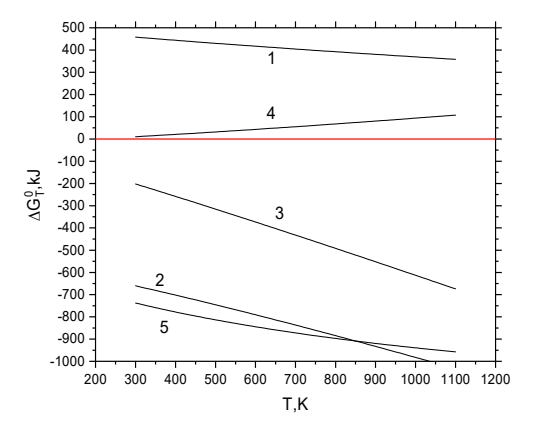


**Fig. 4.** Temperature dependence of the Gibbs free energy for reactions 1-5 at 310-1110 K: 1-eq.1a; 2 - eq.4a; 3 - eq.3a; 4 - eq.2a; 5 - eq.5a

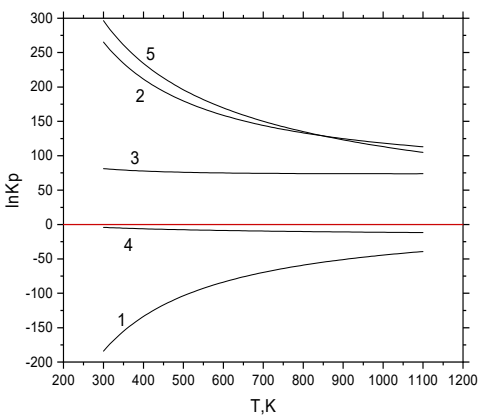


**Fig. 5.** Temperature dependence of the logarithmic values of the equilibrium constant for reactions 1-5 at 310-1110 K: 1 - eq.1b; 2 - eq.4b; 3 - eq.3b; 4 - eq.2b; 5 - eq.5b

The plotted data demonstrate that reactions (2), (3), and (5) proceed in the direction of product formation. These reactions are exothermic and are accompanied by an increase in entropy, which is explained by the increase in the number of gaseous molecules formed. Thermodynamically, the likelihood of pyrolysis reaction (1) resulting in the formation of C<sub>10</sub>H<sub>10</sub> is minimal. Consequently, the transformation of ferrocene into iron is unlikely to occur via the dicyclopentadienyl pathway (reaction 1) and more plausibly proceeds through reaction (3). Additionally, analysis of the Gibbs free energies for reactions (4) and (5) suggests that higher H<sub>2</sub> concentrations significantly enhance the extent of Fe(Cp)<sub>2</sub> reduction, promoting its near-complete conversion.

Thus, it can be concluded that  $\Delta G$  becomes less negative with increasing temperature, which is typical for reactions with negative entropy ( $\Delta S$ <0). At temperatures above ~850–900 K,  $\Delta G$  may become zero or positive, indicating that the reaction becomes thermodynamically unfavorable at these temperatures.

The above results allow for some conclusions regarding the temperature regime of the reaction: the reaction is thermodynamically favorable at T<600 K (~323°C):  $\Delta$ G<0, Keq>>1, especially in the range of 573–773 K (300–500°C), where maximum selectivity for the primary products of ferrocene thermal decomposition is achieved. The reaction is kinetically limited at low temperatures; without a catalyst, the reaction proceeds slowly, and a catalyst is required to lower the Gibbs free energy for the transition state  $\Delta$ G<sup>‡</sup>. At T > 973 K,  $\Delta$ G becomes  $\approx$  0 or slightly > 0, and the value of Keq decreases. The reaction proceeds towards carbonization.

The key stages of the ferrocene hydrogenolysis process are:

1. Initial thermal decomposition of ferrocene (Fc) occurs at T>573 K even without a catalyst and is initiated by heat.

Fc -k<sub>1</sub>
$$\rightarrow$$
 Fe<sup>0</sup> + Hydrocarbons

2. Autocatalytic stage. The formed Fe<sup>0</sup> accelerates the decomposition of the remaining ferrocene:  $Fc+Fe^0-k_2 \rightarrow 2Fe^0+$  Hydrocarbons

3. Formation of iron carbide (Fe<sub>3</sub>C). This occurs upon the saturation of Fe with carbon atoms (from C<sub>5</sub>H<sub>6</sub>, CH<sub>4</sub>, C<sub>2</sub>H<sub>2</sub>):

$$3Fe^0+C-k_3 \rightarrow Fe_3C$$

Below are the differential equations for describing the kinetics of ferrocene hydrogenolysis with autocatalysis:

- Decomposition of ferrocene:  $d[Fc]/dt = -k_1[Fc]-k_2[Fc][Fe]$ ;
- Growth of metallic iron:  $d[Fe]/dt = k_1[Fc]+k_2[Fc][Fe] 3k_3[Fe]_3[C]$ ;
- Formation of Fe<sub>3</sub>C: d[Fe<sub>3</sub>C]/dt=k<sub>3</sub>[Fe]<sub>3</sub>[C];
- Carbon deposition (during hydrocarbon fragmentation):

$$d[C]/dt = \alpha \cdot (k_1[Fc] + k_2[Fc][Fe]) - k_3[Fe]_3[C];$$

[Fc] – concentration of ferrocene, [Fe] – concentration of nano-Fe, [Fe<sub>3</sub>C], [C] – carbide and free carbon. α – stoichiometric coefficient for carbon formation.

The results of the numerical solution of the system of the above differential equations for the hydrogenolysis of ferrocene with autocatalysis are shown in Fig. 6.

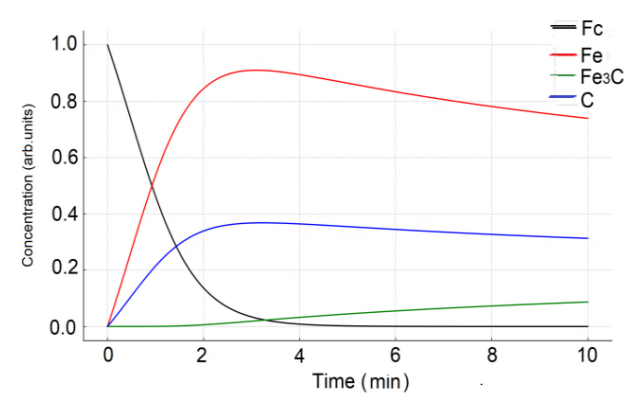


**Fig. 6.** Results of the numerical solution of the system of differential equations for the hydrogenolysis of ferrocene with autocatalysis: [Fc] (black) – exponentially decreases, especially sharply after the appearance of Fe<sup>0</sup>. [Fe] (red) – rises sharply due to autocatalysis → reaches a maximum, then decreases as Fe<sub>3</sub>C forms. [Fe<sub>3</sub>C] (green) – slowly and steadily accumulates as Fe is saturated with carbon. [C] (blue) – initially accumulates, then slightly stabilizes as a balance is reached between formation and consumption.

Thus, it can be concluded that the model accurately reflects the autocatalytic acceleration. The growth of  $Fe \rightarrow$  accelerates the decomposition of Fc, with competition between  $Fe_3C$  and C, which is critical when selecting reaction conditions. It should be noted that the formation of  $Fe_3C$  is a significant, but not predominant, pathway, especially under moderate carbon saturation. This proportion may increase with higher temperature, excess hydrocarbons, or longer reaction times.

Fig. 7 shows the solid product characterization obtained from the thermal decomposition of Fe(Cp)<sub>2</sub>, by X-ray diffraction (a) and FMR spectroscopy (b).

The XRD pattern and FMR spectrum presented are characteristic of samples containing iron-carbon nanoparticles [31, 32]. These diffraction peaks correspond to specific reflections of the metallic Fe phase (PDF #06-0696, BCC structure) and the iron carbide phase. (PDF #35-0772, orthorhombic structure). In the product obtained from the reaction, the peak observed at 44.7° corresponds to the (110) reflection of BCC iron. The grain size, determined using the Scherrer equation, is found to be 11 nm.

The prominent peak observed at 43.4°, corresponding to a grain size of 8 nm, is likely attributed to the (210) reflection of the iron carbide phase.

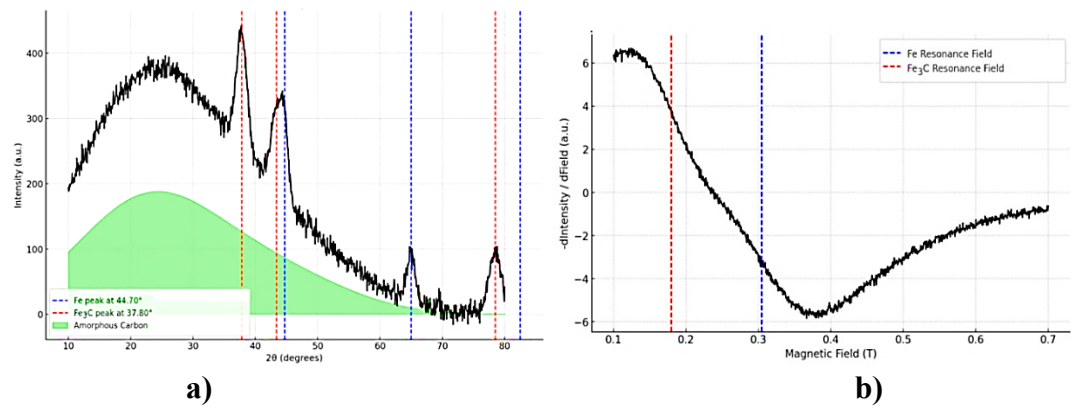


**Fig. 7.** The X-ray diffraction pattern (a) and FMR spectrum (b) represent the solid product formed from the thermal decomposition of Fe(Cp)<sub>2</sub> in a nitrogen (inert gas) flow. In panel (a), blue dashed lines indicate the diffraction peaks for metallic iron (Fe), red dashed lines correspond to iron carbide (Fe<sub>3</sub>C), and the green shaded area reflects the presence of amorphous carbon. In panel (b), blue dashed lines show the resonance field typical of Fe nanoparticles, while red dashed lines represent the resonance field associated with Fe<sub>3</sub>C nanoparticles.

Table 3. Results of Crystallite Size and Microstrain

Phase	Crystallite Size (nm)	$Microstrain(\mathcal{E})$
Fe	10.95	$2.03 \times 10^{-4}$
Fe <sub>3</sub> C	8.49	$1.11 \times 10^{-3}$

These results suggest the coexistence of both Fe and Fe-C nanoparticles in the sample. It is important to highlight that the Fe-C phases are metastable and could decompose into Fe and carbon residues at elevated temperatures. The diffraction pattern reveals specific peaks with Miller indices for Fe: (110),  $2\theta \approx 44.7^{\circ}$ ; (200),  $2\theta \approx 65.0^{\circ}$ ; (211),  $2\theta \approx 82.5^{\circ}$ ; and for iron carbide: (021),  $2\theta \approx 37.8^{\circ}$ ; (210),  $2\theta \approx 43.4^{\circ}$ ; (002),  $2\theta \approx 78.5^{\circ}$ . The refined data for Fe and Fe<sub>3</sub>C, determined using the Williamson-Hall method, are summarized in Table 4.

In addition to X-ray diffraction analysis, the solid products resulting from the thermal decomposition of ferrocene were also examined using ferromagnetic resonance (FMR). The FMR spectrum, recorded at room temperature and presented in Fig. 7b, represents a combined signal from iron nanoparticles, iron carbide, and amorphous carbon. The spectra were modeled using the Landau-Lifshitz-Gilbert equation, taking into account the sample composition and the size of iron, iron carbide, and carbon nanoparticles. These simulated spectra were then compared and fitted to the experimental data for accuracy [33, 34]. During heating, ferrocene readily sublimates and condenses on the inner walls of the reactor, where it subsequently decomposes. The formation mechanism of iron nanoparticles through ferrocene's thermal decomposition involves several critical steps: the breakdown of ferrocene molecules (Fe(C<sub>5</sub>H<sub>5</sub>)<sub>2</sub>), followed by the condensation of free iron atoms into nanoparticles. Under appropriate conditions, the nanoparticle surfaces may become stabilized through the adsorption of hydrocarbon fragments produced during ferrocene decomposition. These carbonaceous residues can form a protective coating around the particles, preventing their aggregation. Consequently, iron nanoparticles encapsulated in a carbon shell are formed, which acts as a passivation layer that protects against oxidation and particle adhesion. Depending on the synthesis parameters, this carbon shell may consist of amorphous carbon or graphite-like material. The size of the iron particles formed during the thermal decomposition of ferrocene depends on many factors: the atmosphere, temperature, nucleation and growth rates, the presence of reducers, catalysts, and the distribution of carbon. Below is Table 4 comparing the particle sizes formed during the hydrogenolysis and pyrolysis of ferrocene.

T 11 4 C '	C1 1	1 ' 1	1 ' '	( CC +	.1	C' 4' 1 '
<b>Table 4</b> . Comparison	of hydrogeno	dvsis and nv	olysis reactions	(effect on	i the size (	of iron particles

Parameter	Hydrogenolysis (in H <sub>2</sub> )	Pyrolysis (in Ar/N <sub>2</sub> )
Medium	Reducing	Inert (sometimes slightly oxidative)
Temperature	573–873 K	873–1173 K
Form of Fe	Reduction of $Fe^{2+} \rightarrow Fe^0$ (smooth	Slow release of Fe <sup>0</sup> through
deposition	nucleation)	thermolysis
Crystallite growth	Moderate: H <sub>2</sub> "smooths" the	Increased: due to aggregation and
rate	growth	absence of H <sub>2</sub>
Carbon formation	Partially suppressed, carbon is	Carbon $\rightarrow$ graphite/soot-like shell,
	evenly distributed	inhibits growth
Fe <sub>3</sub> C formation	Moderate (~20–30%)	Predominant (~40–60%)

Another question arises: Which case produces larger iron particles? In the case of hydrogenolysis, typical iron particle sizes are 8-20 nm (regular, uncoated), whereas in pyrolysis they are 2-10 nm, mostly encapsulated in carbon. So why does pyrolysis result in smaller particles? Most likely, the smaller particle size in pyrolysis is due to higher temperatures inducing intense nucleation but limited growth, the formation of a carbon shell (core-shell structure) inhibiting further growth, and the restriction of iron growth by the formation of Fe<sub>3</sub>C and a passivating carbon layer.

Hydrogenolysis of ferrocene leads to larger iron particles, whereas pyrolysis forms smaller and encapsulated iron nanoparticles (or Fe<sub>3</sub>C), mostly covered by a carbon shell. In hydrogenolysis (in H<sub>2</sub>), particles grow faster and reach up to 20 nm due to smoother nucleation and active growth. In pyrolysis (in an inert gas flow), particle size increases slowly, not exceeding 10 nm, due to the carbon coating and restricted growth. Fig.s 8 and 9 show the cumulative distribution function (CDF) and lognormal distribution curves of iron particle sizes for the hydrogenolysis and pyrolysis processes of ferrocene, respectively.

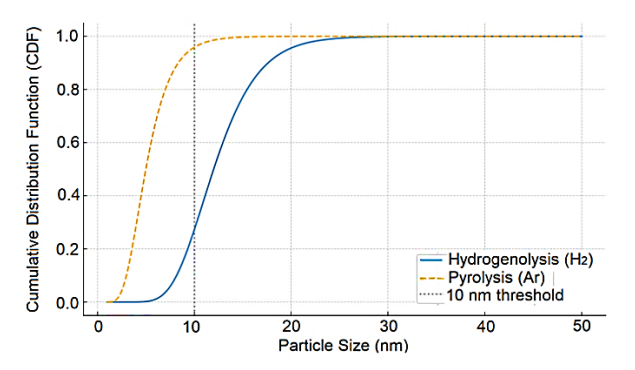


**Fig. 8.** Distribution function (CDF): Hydrogenolysis – the curve grows slowly→ more large particles; Pyrolysis (in an inert gas flow) – rapid saturation of the CDF→ the majority of particles are in the 2–8 nm range. The vertical line at 10 nm clearly shows that in hydrogenolysis, approximately 73% of particles exceed 10 nm, whereas in pyrolysis, only about 4% exceed 10 nm.

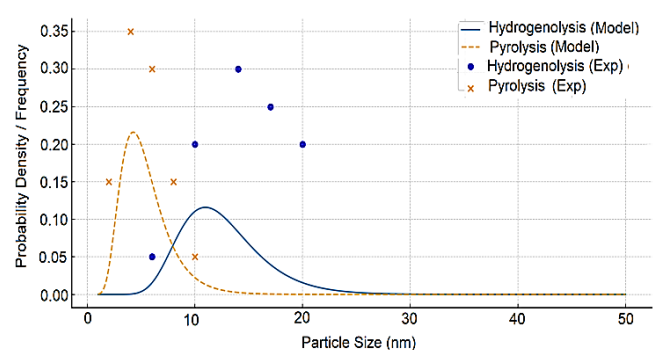


**Fig. 9.** Log-normal distribution curves of iron particles: Hydrogenolysis (black curve) – peak at 12 nm, narrow distribution, typical of thermodynamically controlled growth; Pyrolysis (orange curve) – peak at 5 nm, broader distribution, indicating uneven nucleation and encapsulation in carbon.

According to the log-normal model, the proportion of iron particles exceeding 10 nm during hydrogenolysis is approximately 72.8%, indicating that hydrogenolysis promotes the formation of predominantly larger and more stable nanoparticles, especially at temperatures above 773 K. Experimentally, hydrogenolysis shows a size maximum around 14–17 nm, which aligns well with the model prediction (scale=12). For pyrolysis, the experimental size distribution is centered around 4–6 nm, also consistent with the model (scale=5). Size estimates from the Scherrer equation (XRD) are

 $D_{hydro} \approx 16.0$  nm and  $D_{pyro} \approx 5.3$  nm, which agree well with the distributions calculated from the probabilistic model. The Fe<sub>3</sub>C particle size distribution is modeled as log-normal with scale  $\approx 8$ ,  $\sigma = 0.35$ , peaking at 7–9 nm, which fits cases where iron becomes saturated with carbon, potentially forming iron carbide (Fe<sub>3</sub>C). According to the log-normal model ( $\sigma = 0.35$ , mean  $\approx 8$  nm), the proportion of Fe<sub>3</sub>C particles exceeding 10 nm is 26.2%. In contrast, the share of particles >10 nm in pyrolysis is just 4.2%, confirming that the vast majority of particles remain below 10 nm, which is consistent with experimental observations of encapsulated, finely dispersed Fe<sup>0</sup>/Fe<sub>3</sub>C particles.

Table 5 presents the kinetic model of iron particle growth in the case of hydrogenolysis and pyrolysis of ferrocene.

**Table 5.** Kinetic Model of Fe<sup>o</sup> Particle Growth in the Case of Hydrogenolysis and Pyrolysis of Ferrocene

Process	Growth Model	Result
Hydrogenolysis	$(dR/dt) \propto (1/R)$	Gradual coarsening (growth with deceleration)
Pyrolysis	$(dR/dt) \propto e^{-aR}$	Growth quickly saturates (~5–6 nm)

In hydrogenolysis, the particle radius increases over time, whereas in pyrolysis, growth is rapidly blocked (due to carbon passivation and surface saturation).

Fig. 10 shows the particle growth curves for iron in the hydrogenolysis and pyrolysis of ferrocene at various temperatures.

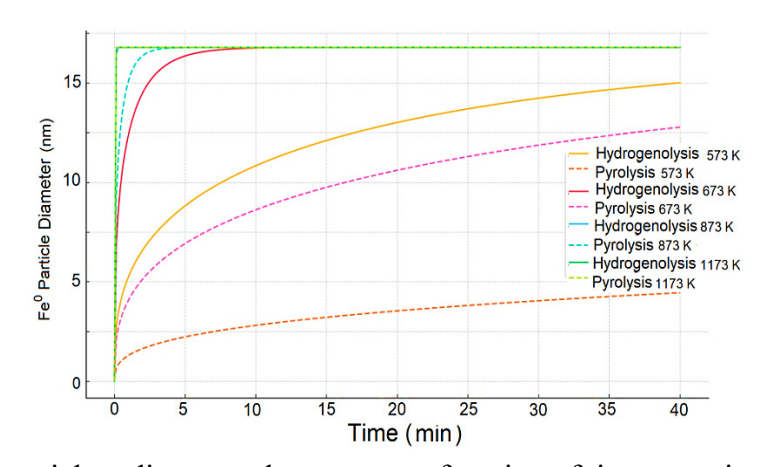


Fig. 10. Iron particle radius growth curves as a function of time at various temperatures.

In pyrolysis (dashed lines), the activation energy is higher. In the 573–773 K range, particle growth is significantly limited (diameter < 5 nm), while at temperatures above 873 K, particle growth accelerates considerably. Even at 573 K, the particle diameter reaches approximately 6–7 nm within ~15 min. At the same ferrocene decomposition time, particle growth is faster during hydrogenolysis, especially at lower temperatures.

#### 4. Conclusion

Ferrocene is one of the most widely used precursors for the synthesis of carbon nanotubes (CNTs) and iron-based catalysts with controlled sizes of active components. Understanding the mechanism of its decomposition under different reaction conditions is necessary to control the product composition. Intermediates formed during the decomposition can promote CNT growth, act as carbon sources, or hinder the process by forming volatile or polyaromatic hydrocarbons that deactivate the catalytic iron species. Determination of the key reaction steps and identification of the resulting intermediates and final products is of paramount importance. Our and currently available results show that the composition of the gas-phase products, as well as the composition, structure, and particle size of the solid products of thermal reduction of ferrocene, depend significantly on the

reaction conditions. Therefore, the study of the chemistry of thermal decomposition of ferrocene requires the primary use of *in situ* chromatography-mass spectrometry in combination with X-ray diffractometry, optical spectroscopy, and magnetic resonance. From a fundamental point of view, ferrocene hydrogenolysis is a rare case of reactions occurring with the cleavage of the Fe-C bond at moderate temperatures, which allows studying the strength of  $\sigma$ -bonds between the metal and cyclopentadienyl ligands, the mechanism of cleavage of metallocene bonds, the effect of the decomposition medium and the role of iron particles as a catalyst. The resulting iron particles play a catalytic role in further decomposition, and this is a unique case of a self-accelerating, i.e. autocatalytic, reaction. Finally, ferrocene hydrogenolysis turns out to be a very convenient model reaction for studying the nucleation and growth of metal nanoparticles and their interaction with hydrogen and organic residues. From a practical point of view, ferrocene hydrogenolysis turns out to be a good basis for developing methods for the synthesis of iron nanoparticles, catalysts on oxide, zeolite, etc., bases with a controlled size of iron particles.

#### References

- 1. Werner H. At least 60 years of ferrocene: the discovery and rediscovery of the sandwich complexes. *Angewandte Chemie*. 2012, **Vol. 51(25)**, p. 6052-6058. <a href="https://doi.org/10.1002/anie.201201598">https://doi.org/10.1002/anie.201201598</a>
- 2. Phillips E.S. Ferrocenes: compounds, properties and applications. Chemical engineering methods and technology. Nova Science Publishers. 2011. 411 p.
- 3. Islam S., Wang F. A comparative study of energetics of ferrocenium and ferrocene. Preprints, 2018. <a href="https://doi.org/10.20944/preprints201808.0166.v1">https://doi.org/10.20944/preprints201808.0166.v1</a>
- 4. Deng Ya-Ru., Li Ya-Fei., Yang H., Fan Yan-Ru., Huang Y. Synthesis, DNA binding of bisnaphthyl ferrocene derivatives and the application as new electroactive indicators for DNA biosensor. *J. Inorg. Biochem.* 2024, **Vol. 257**. Art. 112615. https://doi.org/10.1016/j.jinorgbio.2024.112615
- 5. Lee W., Li L., Camarasa-Gómez M., Hernangómez-Pérez D., Roy X., Evers F., Inkpen M.S., Venkataraman L. Photooxidation driven formation of Fe-Au linked ferrocene-based single-molecule junctions. *Nat Commun.* 2024. **Vol. 15**. Art. 1439. <a href="https://doi.org/10.1038/s41467-024-45707-z">https://doi.org/10.1038/s41467-024-45707-z</a>
- Zhuk Yu.Yu., Strizhakova N.G., Maletin Y.A. Ferrocene-containing ligands in the self-assembly of trinuclear μ<sub>3</sub>-oxocentered carboxylate complexes of chromium (III, III, III)carboxylate complexes of chromium(III, III, III). *Theor Exp Chem.* 2000, Vol. 36. p. 215–219. <a href="https://doi.org/10.1007/BF02522754">https://doi.org/10.1007/BF02522754</a>
- 7. Hassan A., Zafar H.K., Nafady A., Sohail M. Synthesis and characterization of novel ferrocene/PbS nanocomposite material by low-temperature co-precipitation method. *Inorg. Chem. Commun.* 2024, **Vol. 162**. Art. 112194. <a href="https://doi.org/10.1016/j.inoche.2024.112194">https://doi.org/10.1016/j.inoche.2024.112194</a>
- 8. Rauf U., Shabir G., Bukhari S., Albericio F., Saeed A. Contemporary Developments in Ferrocene Chemistry: Physical, Chemical, Biological and Industrial Aspects. *Molecules*. 2023, Vol. 28(15), Art. 5765. <a href="https://doi.org/10.3390/molecules28155765">https://doi.org/10.3390/molecules28155765</a>
- 9. Xu M., Wu C., Zhang F., Zhang Y., Ren J., Zhang C., Wang X., Xiao L., Fontaine O., Qian J. Potential regulation strategy enables ferrocene as p-type redox mediator for direct regeneration of spent LiFePO<sub>4</sub> cathode. *Energy Storage Materials*. 2024, **Vol. 71**, Art. 103611. https://doi.org/10.1016/j.ensm.2024.103611
- 10. Larik F.A., Saeed A., Fattah T.A., Muqadar U., Channar P.A. Recent advances in the synthesis, biological activities and various applications of ferrocene derivatives. *Appl. Organomet. Chem.* 2017, **Vol. 31**, 3664. <a href="https://doi.org/10.1002/aoc.3664">https://doi.org/10.1002/aoc.3664</a>
- 11. Elessawy N.A., Elnouby M., Gouda M.H., Hamad H.A., Taha N.A., Gouda M., Mohy Eldin M.S. Ciprofloxacin removal using magnetic fullerene nanocomposite obtained from sustainable PET bottle wastes: Adsorption process optimization, kinetics, isotherm, regeneration and recycling

- studies. *Chemosphere* 2020, **Vol.** 239, Art. 124728. <a href="https://doi.org/10.1016/j.chemosphere.2019.124728">https://doi.org/10.1016/j.chemosphere.2019.124728</a>
- 12. Wulan P.P.D.K., Sinaga T.E. The effect of iron-carbon ratio and on carbon nanotube synthesis using camphor and ferrocene as carbon sources in the gauze reactor. *S. Afr. J. Chem. Eng.* 2021, **Vol. 36**. p. 17-23; <a href="https://doi.org/10.1016/j.sajce.2020.12.001">https://doi.org/10.1016/j.sajce.2020.12.001</a>
- 13. Kelly C.H.W., Lein M. Choosing the right precursor for thermal decomposition solution-phase synthesis of iron nanoparticles: tunable dissociation energies of ferrocene derivatives. *Phys. Chem. Chem. Phys.* 2016, **Vol. 18(47)**, p. 32448-32457. <a href="https://doi.org/10.1039/C6CP06921E">https://doi.org/10.1039/C6CP06921E</a>
- 14. Rooj A., Roy M., Bhattacharjee A. Thermal Decomposition Reaction of Ferrocene in the Presence of Oxalic Acid. *International Journal of Chemical Kinetics*. 2017, **Vol. 49(5)**, p. 319-332. https://doi.org/10.1002/kin.21077
- 15. Chen, BY., Chi, CC., Hsu, WK. *et al.* Synthesis of SiC/SiO<sub>2</sub> core—shell nanowires with good optical properties on Ni/SiO<sub>2</sub>/Si substrate via ferrocene pyrolysis at low temperature. *Sci Rep.* 2021, **Vol. 11**, Art. 233. <a href="https://doi.org/10.1038/s41598-020-80580-y">https://doi.org/10.1038/s41598-020-80580-y</a>
- 16. Hussain A., Murashko K., Tsapenko A.P., Ding E.-X., Kauppinen E.I., Lähde A.Single-Step Fabrication of Iron Single-Walled Carbon Nanotube Film from Ferrocene as a Conductive-Electrocatalyst Interlayer in Lithium–Sulfur Batteries. *J. Phys. Chem. C.* 2023, Vol. 127(49), p. 23577-23585. <a href="https://doi.org/10.1021/acs.jpcc.3c05777">https://doi.org/10.1021/acs.jpcc.3c05777</a>
- 17. Ivanovskaya V.V., Ivanovskii A.L. Quantum-chemical modelling of composite nanomaterials: Iron clusters Fe<sub>n</sub> (n = 6, 15, 19) in carbon nanotubes. *Theor. Exp. Chem.*, 2006, **Vol. 42**, p. 239–244. https://doi.org/10.1007/s11237-006-0046-z
- 18. Loedolff M.J., Fuller R.O., Nealon G.L., Saunders M., Spackman M.A., Koutsantonis G.A. Solution-phase decomposition of ferrocene into wüstite-iron oxide core–shell nanoparticles. *Dalton Trans.*, 2022, Vol. 51, p. 1603-1611. <a href="https://doi.org/10.1039/D1DT03222D">https://doi.org/10.1039/D1DT03222D</a>
- 19. Ivantsov M., Krysanova K., Grabchak A., Kulikova M. Hydrogenation of CO in the Presence of Fe-Containing Materials Based on Carbon Supports. *Eurasian Chemico-Technological Journal*, 2022, Vol. 24(4), p. 303–311. <a href="https://doi.org/10.18321/ectj1474">https://doi.org/10.18321/ectj1474</a>
- 20. Bhattacharjee A., Rooj A., Roy D., Roy M. Thermal decomposition Study of Ferrocene [(C<sub>5</sub>H<sub>5</sub>)<sub>2</sub>Fe]. *Journal of Experimental Physics*, 2014, Art. 513268, 8 pages. https://doi.org/10.1155/2014/513268
- 21. Kundu S., Sarkar T., Ghorai G., Sahoo P.K., Al-Ahmadi A.A., Alghamdi A., Bhattacharjee A. Reaction Atmosphere-Controlled Thermal Conversion of Ferrocene to Hematite and Cementite Nanomaterials-Structural and Spectroscopic Investigations, *ACS Omega*, 2024, Vol. 9(21), p. 22607-22618. <a href="https://doi.org/10.1021/acsomega.3c10332">https://doi.org/10.1021/acsomega.3c10332</a>
- 22. Grimm S., Hemberger P., Kasper T., Atakan B. Mechanism and Kinetics of the Thermal Decomposition of Fe(C<sub>5</sub>H<sub>5</sub>)<sub>2</sub> in Inert and Reductive Atmosphere: A Synchrotron-Assisted Investigation in A Microreactor. *Advanced Materials Interfaces*, 2022, **Vol. 9(22)**, Art.2200192 <a href="https://doi.org/10.1002/admi.202200192">https://doi.org/10.1002/admi.202200192</a>
- 23. Kuwana K., Saito K. Modeling ferrocene reactions and iron nanoparticle formation: Application to CVD synthesis of carbon nanotubes. *Proceedings of the Combustion Institute*. 2007, **Vol.** 31(2), p. 1857-1864. <a href="https://doi.org/10.1016/j.proci.2006.07.097">https://doi.org/10.1016/j.proci.2006.07.097</a>
- 24. Rustamova A.I., Gurbanov Z.G., Mammadova Z.M., Osmanova S.N., Guluzade A.Kh., Mammadov A.N., Ismailov E.H. Thermal stability and thermodynamics of pyrolysis of mono, bi-, and trinuclear carbinol derivatives of ferrocene. *Chemical Problems*, 2023, Vol. 21(3), p. 251-261. <a href="https://chemprob.org/wp-content/uploads/2023/08/251-261.pdf">https://chemprob.org/wp-content/uploads/2023/08/251-261.pdf</a>
- 25. Orudzhev F.F., Alikhanov N.M.-R., Ramazanov S.M., Sobola D.S., Murtazali R.K., Ismailov E.H., Gasimov R.D., Aliyev A.Sh., Ţălu Ş. Morphotropic Phase Boundary Enhanced Photocatalysis in Sm Doped BiFeO<sub>3</sub>. *Molecules*. 2022, **Vol. 27**, 7029. <a href="https://doi.org/10.3390/molecules27207029">https://doi.org/10.3390/molecules27207029</a>
- 26. Rustamova A.I, Muradxanov R.M, Osmanova S.N., Pashayeva F.K., Mammadov A.N., Tagiyev D.B., Ismailov E.H. Heteronuclear Fe-Mn Cyclopentadienyl Complexes Supported on Boehmite.

- Thermochemistry and Thermodynamics of their Decomposition. *Eurasian Chem.-Technol. J.* 2024. Vol. 26(3), p. 161–168. https://doi.org/10.18321/ectj1639
- 27. Mishenko K.P., Ravdel A.A. *Concise Handbook of Physico-Chemical Quantities*. Leningrad: Khimiya. Seventh Edition. 1974, 200 p. <a href="https://studylib.ru/doc/6242384/kratkij-spravochnik-fiziko-himicheskih-velichin.-pod-red">https://studylib.ru/doc/6242384/kratkij-spravochnik-fiziko-himicheskih-velichin.-pod-red</a>
- 28. Database of thermal constants of substances. Electronic version edited by Iorish V.S. and Yungman V.S. 2006. <a href="https://www.chem.msu.ru/cgi-bin/tkv.pl?show=welcome.html">https://www.chem.msu.ru/cgi-bin/tkv.pl?show=welcome.html</a>
- 29. Haynes W.M., Lide D.R., Bruno T.J. eds. *CRC handbook of chemistry and physics: a ready-reference book of chemical and physical data* (2016-2017, 97th ed.). Boca Raton. Florida. CRC Press. ISBN 978-1-4987-5428-6. OCLC 93068194
- 30. Vančik H. *Basic Organic Chemistry for the Life Sciences*. Springer. 2014. 179 p. <a href="https://tech.chemistrydocs.com/Books/Organic/Basic-Organic-Chemistry-for-the-Life-Sciences-by-Hrvoj-Van%C4%8Dik.pdf">https://tech.chemistrydocs.com/Books/Organic/Basic-Organic-Chemistry-for-the-Life-Sciences-by-Hrvoj-Van%C4%8Dik.pdf</a>
- 31. Khurshid H., Abdu Y.A., Devlin E., Issab B.A., Hadjipanayis G.C. Chemically synthesized nanoparticles of iron and iron-carbides. *RSC Adv.*, 2020, **Vol. 10**, p. 28958-28964. <a href="https://doi.org/10.1039/D0RA02996C">https://doi.org/10.1039/D0RA02996C</a>
- 32. Hseih C.T., Huang W.L., Lue J.T. The change from paramagnetic resonance to ferromagnetic resonance for iron nanoparticles made by the sol–gel method. *J. of Physics and Chemistry of Solids*. 2002, Vol. 63, p. 733–741. https://doi.org/10.1016/S0022-3697(01)00222-0
- 33. Chalapat K., Timonen J.V.I., Huuppola M., Koponen L., Johans C., Ras R.H.A., Ikkala O., Oksanen M.A, Seppälä E., Paraoanu G.S. Ferromagnetic resonance in ε-Co magnetic composites. *Nanotechnology*, 2014, **Vol. 25(48)**, 485707. <a href="https://doi.org/10.1088/0957-4484/25/48/485707">https://doi.org/10.1088/0957-4484/25/48/485707</a>
- 34. Rustamova A.I., Muradkhanov R.M., Osmanova S.N., Soloviev S.O., Ismailov E.H. Effect of calcination temperature on the phase composition and magnetic properties of the boehmite with adsorbed ferrocene. *Chemical Problems*, 2025, **Vol. 1(23)**, p. 107–115. DOI 10.32737/2221-8688-2025-1-107-115